Long-time-scale dynamics observed in directional solidification of a binary alloy

Konstantinos Tsiveriotis and Robert A. Brown
Department of Chemical Engineering, Massachusetts Institute of Technology, Cambridge, Massachusetts 02139
(Received 3 March 1993; revised manuscript received 27 December 1993)

Asymptotic analysis and finite-element simulations are used to explore the nonlinear dynamics present in cellular interface patterns that arise in thin-film directional solidification, as caused by the presence of a codimension-two bifurcation at a specific value of the spatial wavelength for the cells. For certain parameter sets, the quadratic nonlinearities that dominate the dynamics because of 2:1 spatial resonance give rise to secondary steady-state bifurcation and to time-periodic states with periods that scale as $\delta^{-3/2}$, where δ measures the distance from the parameter values for the codimension-two state. The structure of this dynamics is explored in closed form for a modified Swift-Hohenberg equation and for the two-sided, solutal model for directional solidification. The asymptotic results for directional solidification are verified by finite-element numerical simulations for small amplitude cells.

I. INTRODUCTION

There is increasing experimental and computational evidence that the shallow two-dimensional cellular structures formed just after the onset of morphological instability in directional solidification of a binary alloy exhibit spatiotemporal chaos on long-time scales compared to the characteristic diffusion times for solute and heat in the system. The purpose of this paper is to show that the appearance of long-time-scale dynamics in directional solidification systems is, at least, partially predictable because of the flatness of the neutral stability curve associated with the linear instability of the planar state and because of temporal dynamics produced from interactions of spatially resonant wavelengths for growth conditions very close to the onset of the transition from planar to cellular interface structures.

In the thin-film solidification of a dilute binary alloy considered here, cellular microstructures begin as an instability to the planar interface for solidification rates V above a critical value $V=V_c$. This critical value is given by the neutral stability curve from linear stability analysis[1] as $V=V_c(\omega)$, where ω is the wave number of the disturbance along the lateral dimension of the planar interface. For $V>V_c$, a range of wave numbers are linearly unstable. Weakly nonlinear bifurcation analysis and numerical simulations confirm that, for each value of the wavelength a family of steadily solidifying, finite amplitude cells evolve, either subcritically or supercritically with changing V from $V_c(\omega)$.[2-5] Theory and numerical simulations have established that the presence of this band of wave numbers and the nonlinear interactions between these states, causes no single value of the wavelength to be selected as the microstructure evolves with increasing V.

In fact, even the critical wave number $\omega=\omega_c$ predicted by linear stability theory to correspond to the lowest value of the growth rate $V=V_c(\omega_c)$ for instability is extremely difficult to observe in either experiments or computations with large samples, because the flatness of the neutral stability curve leads to a band of unstable wave numbers for $|V-V_c|\ll 1$. This flatness is a direct result of the small influence of the melt-solid interface free energy in setting the shape of the interface.

The flatness of the neutral stability curve is particularly important because of the importance of nonlinear interactions between both steady and transient cells, which lead to bounds on V for the existence of families of cells with particular wave numbers. This was demonstrated by Ungar and Brown[3] using numerically implemented bifurcation analysis for a model of two-dimensional cellular solidification and was analyzed in detail by Haug[7,8] using techniques from imperfect bifurcation analysis. An important result of these studies was to identify secondary bifurcations that occur between families of cells with spatial wave numbers ω and 2ω. The appearance of these secondary bifurcations is directly linked to the existence of the codimension-two bifurcation that occurs where two families of steady cells evolve from the same value of the growth rate, $V=V_d$ where the two neutrally stable wave numbers are related as ω_d and $2\omega_d$. The amplitude equations presented by Haug[7,8] for describing the nonlinear interactions of the two modes with wave numbers ω_d and $2\omega_d$ were derived as an expansion about the critical value $V=V_d$ and build on the more general theory developed by Dangelmayr and Armbruster;[9,10] also see Ref. 11.

The importance of the nonlinear connectivity between steady-state solution families is great, especially when coupled with the flatness of the neutral stability curve. First, it supplies a mechanism for increasing the wave number above the critical value predicted by linear stability theory, from ω_c to $2\omega_c$ and to larger values for small increases in growth rate, as observed several times[3-5] in computations and seen in recent experiments.[12] Secondly, it severely limits the utility of the predictions of sideband stability analyses of weakly nonlinear states, the so-called Eckhaus analysis,[13,14] by restricting the validity of these results to a range of V above which the secondary bifurcations caused by mode interactions dominate the

evolution of the interface.

Most important to the results presented here, the nonlinear interactions between modes with wave numbers ω and 2ω also may lead to time-dependent states through Hopf bifurcations. Proctor and Jones[15] demonstrated this fact in the derivation of general amplitude equations near a codimension-two bifurcation generated by 2:1 spatial resonance. What is of particular importance is that the Hopf bifurcations caused by the codimension-two bifurcations evolve from the secondary bifurcation point with a period of oscillation that increases toward infinity as the codimension-two point is approached. Thus, for physical systems, like directional solidification, where the neutral stability curve is very flat, the period of the oscillation can be extremely large. This observation follows solely from the fact that for the parameters values for the codimension-two point, no oscillatory instabilities are possible emanating from the neutral stability curve. We demonstrate that this long-time-scale dynamics is very important in the development of microstructure during the directional solidification of a binary alloy.

Chaotic, long-time-scale nonlinear dynamics were observed by Bennett and Brown[5] in numerical simulations of thin-film directional solidification. They demonstrated nonperiodic dynamics in simulations with sample widths corresponding to $4\lambda_c$, where $\lambda_c = 2\pi/\omega_c$. The fundamental mechanism observed in this dynamics was interactions between neighboring cells that lead to tip splitting of an individual cell to form two cells with half of the original width (or twice the wave number) and the lateral migration, growth or dissolution of these new cells in time. Each of these mechanisms is expected from the nonlinear dynamics associated with the Hopf bifurcation caused by the codimension-two structure. The dynamics computed by Bennett and Brown[5] occurred on a time scale of approximately $O(10^3)$ diffusion time units and corresponded to the time scales seen for simpler, time-periodic dynamics observed in calculations for samples that were only one wavelength wide. Motivated by these calculations, Lee and Brown[16] designed a very large, thin-film solidification experiment and observed long-time-scale, chaotic dynamics in the solidification of succinonitrile-acetone alloys. For growth rates very close to $V_c(\omega_c)$, long solidification experiments gave a solidification interface with cells represented by a band of wave numbers, which evolved in time and exhibited nonlinear dynamics between neighboring cells.

The purpose of this paper is to demonstrate the connection between the time scale of the time-periodic states predicted for the codimension-two bifurcation arising from 2:1 spatial resonance and the dynamics observed in thin-film directional solidification, as represented here by the two-sided solutal model for directional solidification used by Bennett and Brown.[5] Because of the complexity of the solutal model, the asymptotic structure of the Hopf bifurcation is first explored for a simpler model problem that displays the same dynamical structure; we use a modification of the Swift-Honenberg[17] equation for this purpose.

Asymptotic analysis about the codimension-two structure is carried out using the center manifold reduction[18–21] to compute the system dynamics using two coupled amplitude equations representing the magnitudes of the two interacting modes. Center manifold analysis constructed about the codimension-two bifurcation provides a very general framework for capturing the dynamics of both the steady-state bifurcating families, the time-periodic states and the long-time-scale dynamics of the oscillatory solutions. This combination involves dynamics both near the primary and secondary bifurcation points and cannot be captured by a simpler perturbation expansion using a single expansion parameter. Multiple perturbation parameters in a multiple-time-scale expansion would be necessary to analyze these dynamics by classical methods. The center manifold approach is more straightforward for this analysis because the amplitude equations derived for the coefficients of the two interacting modes systematically include all couplings between these and other relevant modes without the need for introducing additional scalings. The scaling of the time period for the oscillatory solutions on the distance of the system from the codimension-two point is derived explicitly; these results are presented in the next section. The solutal model is presented in Sec. III. A similar center manifold analysis of the solutal model is summarized in Sec. IV and the results are shown graphically in Sec. V. The comparison between the asymptotic results and numerical simulations for the solutal model are extremely good for low amplitude cells.

II. MODIFIED SWIFT-HONENBERG EQUATION

The importance of quadratic nonlinearities to the dynamics near the codimension-two bifurcation point that corresponds to 2:1 spatial resonance is most easily seen by considering a model fourth-order nonlinear evolution equation modeled after the equation introduced by Swift and Hohenberg.[17] Following our previous analysis of the Eckhaus instability for the Swift-Hohenberg equation,[14] we consider this equation augmented with quadratic terms to yield

$$\frac{\partial u}{\partial t}+\left[\frac{\partial^2}{\partial x^2}+1\right]^2 u-Ru+f\left[\frac{\partial u}{\partial x}\right]^2+gu^2+u^3=0\ , \tag{1}$$

where R is the control parameter and f and g are constants. We refer to Eq. (1) as the modified-Swift-Hohenberg or MSH equation. The additional quadratically nonlinear terms scaled with g and f are introduced into the Swift-Hohenberg equation to represent the effects of quadratic nonlinearities on the solution structure near the codimension-two bifurcation point. Quadratic nonlinearities dominate the changes in solution structure caused by mode coupling, so that these terms represent the most important effects on the solution structure. The form of these nonlinearities was not selected to mimic directly the behavior of the directional solidification problem. However, each term in Eq. (1) is present in the evolution equations that govern the dynamics of directional solidification; this point is addressed again in Sec. II B.

The real-valued solution $u=u(x,t)$ is assumed to satisfy the reflectively symmetric boundary conditions

$$\frac{\partial^3 u}{\partial x^3}=\frac{\partial u}{\partial x}=0\ ,\quad x=0 \text{ and } x=L\ . \tag{2}$$

This equation is in local form, i.e., $u=0$ is a solution for all values of R. Instability of this base state and bifurcation to a steady-state, finite amplitude form is predicted along the neutral stability curve defined by

$$R=R_{\text{crit}}\equiv F(\omega)=(1-\omega)^2\ , \tag{3}$$

where the linear disturbances have the form $\hat{u}(t)\cos(\omega x)$; Eq. (3) has the form plotted in Fig. 1. Codimension-two bifurcation between modes with spatial forms $\cos(\omega_1 x)$ and $\cos(\omega_2 x)$ occur when $2\omega_1=\omega_2$. For a parabolic neutral stability curve this relationship holds only at one particular value of $R=R_d$, which is $R_d=9/25$ for the MSH equation and corresponds to a critical spatial wave number of $\omega=\omega_d\equiv\sqrt{2}/5$. For the choices of control parameter R_d and spatial wave number ω_d or domain size $\lambda=\lambda_d=2\pi/\omega_d$ steady-state solutions with wave numbers ω_d and $2\omega_d$ branch simultaneously from the base state. The existence of the codimension-two point is emphasized in Fig. 1 by plotting the neutral stability curves $R=R_{\text{crit}}(\omega)$ and $R=R_{\text{crit}}(2\omega)$.

The general structure of this codimension-two bifurcation was studied by Dangelmayr and Armbruster[9,10] by considering the domain length to be fixed at λ_d and taking $|R-R_d|\ll 1$, so that both spatial modes have infinitesimal amplitudes and the interactions can be studied by asymptotic analysis. We consider more general spatial interactions between the two modes with wave numbers ω and 2ω by introducing an additional perturbation parameter that measures the distance in λ from the codimension-two value. We consider a perturbation in the domain length defined by

$$\lambda=(1+\delta)\lambda_d\ , \tag{4}$$

where $|\delta|\ll 1$. Then the wave number is perturbed away from the codimension-two value as $\omega=\omega_d/(1+\delta)=(1-\delta)\omega_d+O(\delta^2)$; this choice of perturbation parameter is convenient for direct comparison to numerical simulation. The perturbation parameter is introduced into the differential equation (1) and boundary conditions (2) by making the change of variables $\eta=x/(1+\delta)$ and rewriting Eqs. (1) and (2) as

$$\frac{\partial u}{\partial t}+\left[\frac{1}{(1+\delta)^2}\frac{\partial^2}{\partial\eta^2}+1\right]^2 u-Ru +f\frac{1}{(1+\delta)^2}\left[\frac{\partial u}{\partial\eta}\right]^2+gu^2+u^3=0\ , \tag{5}$$

$$\frac{\partial^3 u}{\partial\eta^3}=\frac{\partial u}{\partial\eta}=0\ ,\quad x=0 \text{ and } x=\lambda_d\ . \tag{6}$$

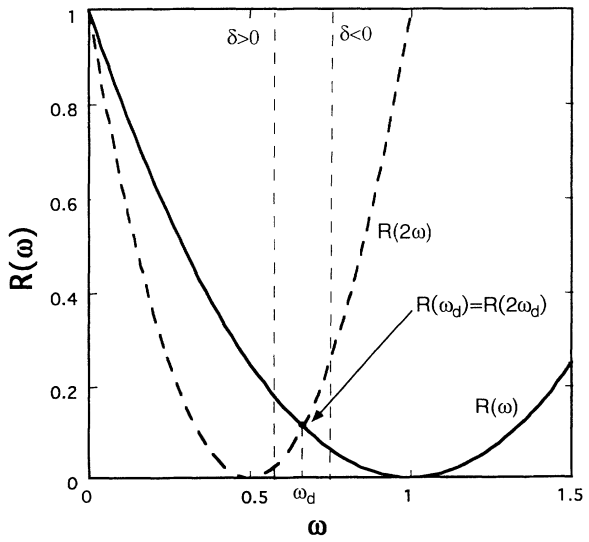

FIG. 1. Schematic of neutral stability diagram showing the codimension-two bifurcation between solutions with spatial frequency ω_d and $2\omega_d$, which occurs at the value of the control parameter $R=R_d$. The paths for the bifurcation diagrams constructed for $\omega<\omega_d$ ($\delta>0$) and $\omega>\omega_d$ ($\delta<0$) are shown as dashed vertical lines.

A. Center manifold reduction

The asymptotic analysis presented here is designed to construct the solutions to Eqs. (5) and (6) in the parameter region $|\delta|\ll 1$ and $r\equiv|R-R_d|\ll 1$. The analysis requires constructing the center manifold for the weakly nonlinear dynamics[18–20] and is based on the fact that near the codimension-two point the entire manifold of the solution dynamics is described by the nonlinear interactions of the two most dangerous spatial modes, with all others decaying exponentially in time to zero. If Eqs. (5) and (6) are considered as a nonlinear evolution equation in local form

$$\frac{\partial u}{\partial t}=L(u)+N(u)\ , \tag{7}$$

where $L(u)$ is a linear operator and $N(u)$ is a nonlinear operator, the linear stability of the trivial solution ($u=0$) has the eigenfunctions $\{q_i(x)\}$, where the first m are members of the null space satisfying $L(q_i(x))=0, i=1,\ldots m$. Construction of the center manifold consists of four steps. First, the weakly nonlinear solution is represented as a linear combination of unknown amplitude coefficients $\{a_i(t)\}$ and the eigenfunctions of L as

$$u(x,t)=\sum_{i=1}^{\infty} a_i(t)q_i(x)\ . \tag{8}$$

Next, Eq. (8) is substituted into Eq. (7) and equations for the amplitude coefficients are formed by projection with respect to the eigenfunctions as

$$\frac{da_i}{dt}=\langle N(u),q_i\rangle, i=1,2,\ldots,m\ , \tag{9}$$

$$\frac{da_i}{dt}=\langle L(u),q_i\rangle a_i+\langle N(u),q_i\rangle, i=m+1,\ldots, \tag{10}$$

where the inner product $\langle\cdot,\cdot\rangle$ is

$$\langle p(x),q(x)\rangle \equiv \int_0^{\lambda_d} p(x)q(x)dx \ . \tag{11}$$

Because the amplitude of the stable modes ($i > m+1$) decay in time, $\partial a_i/\partial t = 0$, $i > m+1$, and Eq. (10) are solved to give these amplitudes in terms of the critical amplitudes ($i+1, \ldots, m$) as

$$a_i = f_i(a_1, a_2, \ldots, a_m), i = m+1, \ldots . \tag{12}$$

These equations are referred to as the *center manifold equations*. Equations (12) are substituted into Eqs. (9) to give dynamical equations written entirely in terms of the critical amplitudes as

$$\frac{da_i}{dt} = F_i(a_1, a_2, \ldots, a_m) \ , \quad i = 1,2,\ldots,m \ . \tag{13}$$

The center manifold construction was applied to the MSH equation to derive a set of amplitude equations valid for $|r| \ll 1$ and $|\delta| \ll 1$. The solution was expressed as a cosine series, as suggested by the boundary conditions, and was substituted into Eq. (5) and expanded to cubic order in the variables $\{a_i\}$, δ and r to yield the amplitude equations for the modes $n = 0,1,2,3,4$. As Proctor and Jones[15] have shown, only these five modes are needed to include all the quadratic and cubic resonant interactions between the critical modes (a_1, a_2).

The equations for (a_0, a_3, a_4) were substituted into the evolution equations for the modes (a_1, a_2) to give the evolution equations

$$\frac{da_1}{dt} = [F'(\omega_d)\omega_d\delta + r]a_1 + b_1 a_1 a_2 + c_1 a_1 a_2^2 + c_2 a_1^3 + O(a_1,a_2)^4 \ , \tag{14a}$$

$$\frac{da_2}{dt} = [F'(2\omega_d)2\omega_d\delta + r]a_2 + b_2 a_1^2 + c_3 a_1^2 a_2 + c_4 a_2^3 + O(a_1,a_2)^4 \ , \tag{14b}$$

where

$$b_1 \equiv 2f\omega^2 + g \ , \quad b_2 \equiv \tfrac{1}{2}g - \tfrac{1}{2}f\omega^2 \ , \tag{15}$$

and the coefficients (c_1, c_2, c_3, c_4) are given in Ref. 22 and are truncated at leading order in the parameters r and δ, because only this dependence plays a role in the remainder of the analysis.

B. Steady-state solutions

Equations (14) admit two nontrivial steady-state solutions. The first contains only a nonzero value of the amplitude a_2; we refer to as the *pure* solution $(a_1^{(p)}, a_2^{(p)})$ with coefficients

$$a_1^{(p)} = 0, a_2^{(p)} = \pm \left[\frac{-r - F'(2\omega_d)2\omega_d\delta)}{c_4} \right]^{1/2} , \tag{16}$$

which exist for

$$[r + F'(2\omega_d)2\omega_d\delta]c_4 < 0 \ , \tag{17}$$

and bifurcates from the trivial solution at

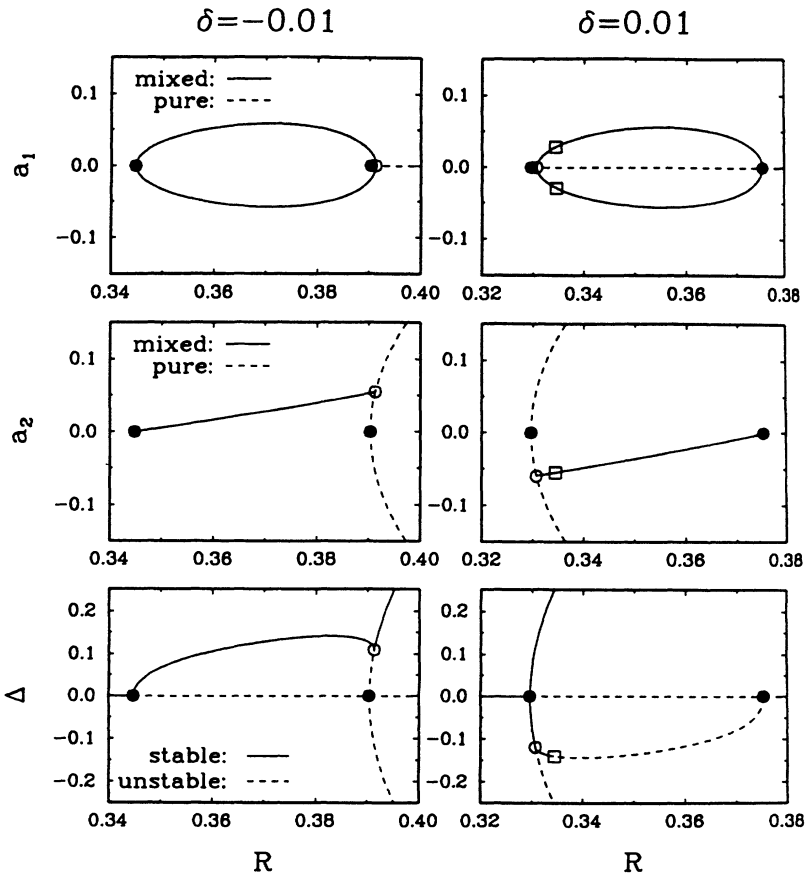

FIG. 2. Parametric structure and linear stability results for the steady-state solutions of the MSH equation with $(f,g)=(1,0)$, i.e., $b_1 b_2 < 0$, as computed from the amplitude equations (14); (a) $\delta = -0.01$ and (b) $\delta = 0.01$. The symbols represent primary (●) and secondary (○) bifurcation points between families of steady-state solutions and (□) Hopf bifurcations to families of time-periodic states. The magnitude of the solution is plotted as $\Delta = |a_1| + |a_2|$.

$$R^{(p)}=R_d-F'(2\omega_d)2\omega_d\delta\ . \tag{18}$$

A second solution contains nonzero values of both amplitudes and is referred to as the *mixed* solution $(a_1^{(m)},a_2^{(m)})$; no closed form expressions exist for this solution, which bifurcates from the trivial state at

$$R^{(p)}=R_d-F'(\omega_d)\omega_d\delta\ . \tag{19}$$

Numerical solutions of Eqs. (14) with the parameters $(f,g)=(1,0)$ and $(f,g)=(0,1)$ are shown in Figs. 2 and 3, respectively. These bifurcation diagrams correspond to the evolution of the solutions in R along the two paths shown in Fig. 1 for each side of the codimension-two point $\omega=\omega_d$. For the first case, the coefficients of the quadratic terms in the amplitude equations have opposite sign, i.e., $b_1b_2<0$, and for the second case these terms are of the same sign, i.e., $b_1b_2>0$. Note that the values of b_1 and b_2 depend on the values of the coefficients f and g in the modified Swift-Hohenberg equation.

When the coefficients are of opposite sign, the two bifurcating solutions are connected, no matter what the sign of δ, the parameter that controls the distance from the codimension-two point. This connectivity is qualitatively different from the simple sequence of unconnected bifurcating families for the Swift-Hohenberg equation[17] and which corresponds to the Eckhaus instability.[14] Alternatively, when $b_1b_2>0$ there is no connectivity between the nontrivial families. While the solution structure is reminiscent of the structure for the original Swift-Hohenberg equation,[14] the family which bifurcates with wave number ω has a contribution from the first harmonic 2ω that increases linearly with r; no such mode coupling is present for the Swift-Hohenberg equation. Clearly the values of the coefficients in the amplitude equations are important to the qualitative predictions of the solution structure. We show in Sec. III that both solution structures predicted with $b_1b_2<0$ and $b_1b_2>0$ occur in directional solidification, depending on the thermophysical properties of the alloy.

The linear stability of the pure and mixed solution families was computed by classical methods and the results are summarized in Figs. 2 and 3. For $b_1b_2<0$ and $\delta<0$, the mixed solution family first bifurcates from the trivial solution and is stable up to a secondary bifurcation point where it connects to the pure solution family. Two branches of the mixed solution appear, each corresponding to a different sign of the value of the coefficient $a_1^{(m)}$. The bifurcation diagram is reversed for $\delta>0$, where the pure solution family branches from the trivial state at the lowest value of R and the mixed solution bifurcates subcritically and connects to the pure family at a secondary bifurcation point. The most interesting qualitative difference between the solution structures with changing the sign of δ, is the appearance of a time-periodic or Hopf bifurcation on the mixed solution family near the secondary bifurcation point. This Hopf point was noted by Haug[7] and Proctor and Jones.[15] Our analysis is focused

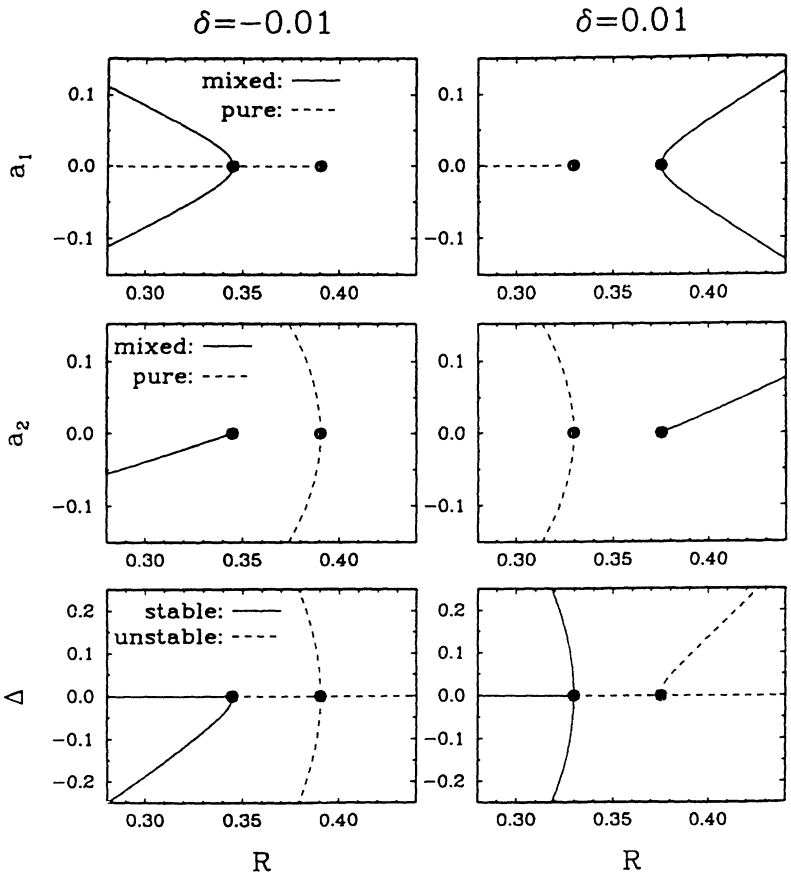

FIG. 3. Parametric structure and linear stability results for the steady-state solutions of the MSH equation with $(f,g)=(0,1)$, i.e., $b_1b_2>0$, as computed from the amplitude equations (14); (a) $\delta=-0.01$ and (b) $\delta=0.01$. The symbols represent primary (●) and secondary (○) bifurcation points families of steady-state solutions and (□) Hopf bifurcations to families of time-periodic states. The magnitude of the solution is plotted as $\Delta=|a_1|+a_2|$.

on the temporal frequency of these time-periodic solutions and on the dependence of the period on the scaling parameters δ and r.

C. Time-periodic solutions

Detailed analysis of the Hopf bifurcation is greatly simplified by closed form results for the mixed solution family and for the linear stability analysis. This can be accomplished by noting that the Hopf point becomes asymptotically close to the secondary bifurcation with the pure solution family as $|\delta| \ll 1$. The cubic terms in Eqs. (14) can be simplified further using this fact. A comparison of the scalings between the two amplitudes near this point suggests that only the cubic term a_2^3 is comparable in magnitude to the quadratic terms near $\delta=0$ and must be retained in the amplitude equations. Hence, Eqs. (14) and (15) reduce to

$$\frac{da_1}{dt} = -[F'(\omega_d)\omega_d\delta - r]a_1 + b_1 a_1 a_2 , \tag{20a}$$

$$\frac{da_2}{dt} = -[F'(2\omega_d)2\omega_d\delta - r]a_2 + b_2 a_1^2 + c_4 a_2^3 . \tag{20b}$$

This simplification of the amplitude equations leads to closed-form expressions for the mixed solution family as

$$a_1^{(m)} = \pm \left[\frac{[-F'(\omega_d)\omega_d\delta - r][-F'(2\omega_d)2\omega_d\delta - r]}{b_1 b_2} - \frac{c_4[-F'(\omega_d)\omega_d\delta - r]^3}{b_1^3 b_2} \right]^{1/2} , \tag{21a}$$

$$a_2^{(m)} = \pm \frac{[-F'(\omega_d)\omega_d\delta - r]}{b_1} , \tag{21b}$$

which exists for

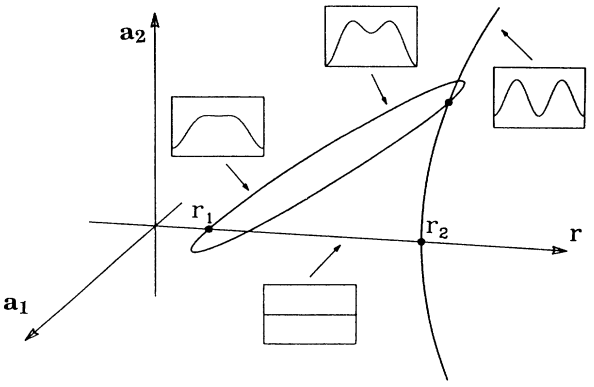

FIG. 4. Schematic diagram of the steady-state solution structure predicted for the amplitude coefficients (a_1,a_2) by the reduced amplitude equations (20) for $b_1 b_2 < 0$, and $\delta < 0$. The bifurcation points, r_1 and r_2, are given as $r_1 = -F'(\omega_d)\omega_d\delta$ and $r_2 = -F'(2\omega_d)2\omega_d\delta$.

$$\frac{[-F'(\omega_d)\omega_d\delta - r][-F'(2\omega_d)2\omega_d\delta - r]}{b_1 b_2} - \frac{c_4[-F'(\omega_d)\omega_d\delta - r]^3}{b_1^3 b_2} > 0 . \tag{22}$$

The expressions for the pure solution remain as Eq. (16). The leading order terms in r and δ describe an ellipse if $b_1 b_2 < 0$ and a parabola if $b_1 b_2 > 0$, thereby giving bifurcating solutions that are consistent with those computed with the full amplitude equations and shown in Figs. 2 and 3; the solution structure predicted by Eqs. (21) and (22) is shown schematically in Fig. 4 for $b_1 b_2 < 0$ and $\delta < 0$.

Using the closed-form solution Eq. (21), the location of the Hopf bifurcation for $b_1 b_2 < 0$ and $\delta < 0$ is computed by linear stability analysis of disturbances with the form $\hat{a}_k e^{\sigma t}$. The two eigenvalues predicted by this analysis are

$$\sigma_{1,2} = -\frac{1}{2}[F'(2\omega_d)2\omega_d\delta + r + 3c_4(a_2^{(m)})^2]^2 \pm \frac{1}{2}\sqrt{[F'(2\omega_d)2\omega_d\delta + r + 3c_4(a_2^{(m)})^2]^2 + 8b_1 b_2 (a_2^{(m)})^2} , \tag{23}$$

These are imaginary only if $b_1 b_2 < 0$ and for r given as the solution of

$$F'(2\omega_d)2\omega_d\delta + r + 3c_4(a_2^{(m)})^2 = 0 , \tag{24}$$

which defines the Hopf point as the value $r = r_{\text{Hopf}}$ where the real part of the eigenvalues vanishes. At the critical value $r = r_{\text{Hopf}}$ the eigenvalues are purely imaginary with an oscillation frequency

$$\Omega = \sqrt{-b_1 b_2 (a_1^{(m)})^2} . \tag{25}$$

Using the closed-form expression for the mixed solution and

$$r = -F'(2\omega_d)2\omega_d\delta + O(r^2, \delta^2, r\delta)$$

as the leading-order approximation to the location of the Hopf point gives

$$\Omega = \left[\frac{-c_4}{b_1^2}[-F'(\omega_d)\omega_d + F'(2\omega_d)2\omega_d]^3\delta^3 \right]^{1/2} . \tag{26}$$

For a parabolic neutral stability curve $F'(\omega_d) < 0$ and $F'(2\omega_d) > 0$, so that Eq. (26) suggests that the Hopf bifurcation only exists for values of δ that satisfy $c_4\delta < 0$; hence, the Hopf bifurcation appears on the mixed branch if $b_1 b_2 < 0$ and only for a specific sign of δ, which depends on the sign of c_4.

Equation (26) predicts that, to leading order, the period of the time-periodic solutions is

$$T \equiv \frac{2\pi}{\Omega} \simeq |\delta|^{-3/2} , \tag{27}$$

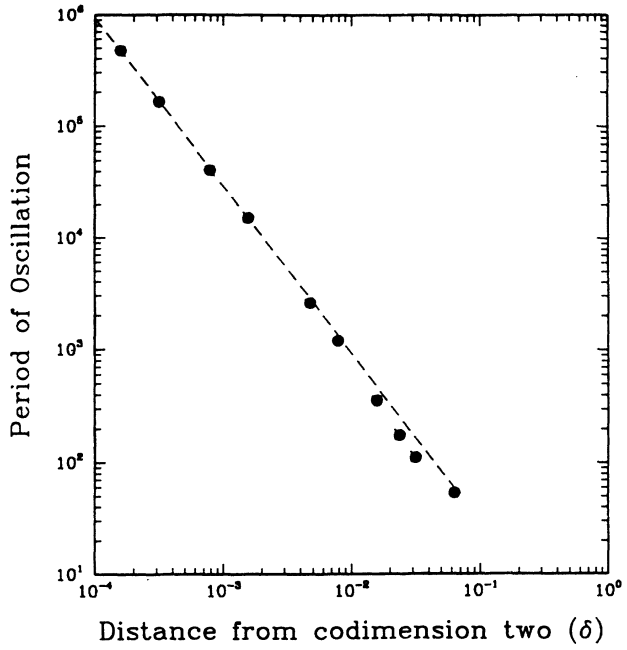

FIG. 5. Period of oscillations computed at the Hopf point as a function of the distance from the codimension-two bifurcation, as measured by δ. Results are shown for the asymptotic expressions, Eq. (27) (— — —), and for numerical solution of the amplitude equations (14) (●).

This is the most important result of the analysis presented here, because it clearly shows a mechanism for the low-time-scale dynamics for a system very close to the codimension-two bifurcation point caused by 2:1 spatial resonance. The relevance of this result to the directional solidification problem and to the dynamics observed by Bennett and Brown is described below. The predictions of the asymptotic analysis for the period of the Hopf bifurcation are compared in Fig. 5 directly to numerical solution of the linear stability problem for the full amplitude equations (14) and (15). The agreement is excellent for $\delta < 0.1$.

III. ANALYSIS OF THE SOLUTAL MODEL OF DIRECTIONAL SOLIDIFICATION

A. The solution model

The solutal model for thin-film solidification of a dilute binary alloy is described in Refs. 5 and 6 and is only repeated here in dimensionless form. Dimensionless variables are formed by scaling lengths with the characteristic wavelength for the cellular interface structure λ_0, temperatures with the melting temperature of the pure material T_m, concentrations with the bulk concentration of the melt far from the interface c_0, and time with the time scale for diffusion in the melt λ_0^2/D_m, where D_m is the diffusivity in the melt. In this model the melt and solid are modeled as having equal thermal conductivities and latent heat release and convective heat transport are neglected. With these assumptions a constant dimensionless temperature gradient G acts in the direction of growth and the temperature field is unaltered by deformation of the interface. When solute diffusion is accounted for in both the melt and solid, the dimensionless solute balances are

$$\nabla^2 c_m + P\frac{\partial c_m}{\partial y} = \frac{\partial c_m}{\partial \tau} \tag{28a}$$

in the melt and

$$R_m \nabla^2 c_s + P\frac{\partial c_s}{\partial y} = \frac{\partial c_s}{\partial \tau} \tag{28b}$$

in the solid, where y is the coordinate direction for growth, τ is the dimensionless time, $R_m \equiv D_s/D_m$ is the ratio of solute diffusivities between solid and melt, and $P \equiv V\lambda_0/D_m$ is the Peclet number or dimensionless translation rate of the sample. The parameter P is used as the control parameter in the analysis and in experiments.

The concentrations of melt and solid are connected at the interface by the relationship for phase equilibrium $c_s = kc_m$, where k is the segregation coefficient, and by the interface solute balance

$$(\mathbf{n}\cdot\nabla c)_m - R_m(\mathbf{n}\cdot\nabla c)_s = (\mathbf{e}_y\cdot\mathbf{n})_m[P + V_e(x,t)](k-l)c_m \ , \tag{29}$$

where $V_e(x,t)$ is the vertical component of the interface velocity in excess of P, $\mathbf{e}_y$ is the unit vector in the y direction and $\mathbf{n}$ is the unit vector normal to the interface. The interface shape is given by the additional constraint of the Gibbs-Thomson condition for interfacial equilibrium:

$$c_{\text{ref}} + \left[\frac{G}{m}\right] y = c_m + \left[\frac{\Gamma}{m}\right] 2H \ , \tag{30}$$

where H is the mean curvature of the two-dimensional interface, m is the slope of the liquidus curve of the phase diagram, Γ is the dimensionless capillary length and c_{ref} is a reference concentration that is fixed at the concentration in the melt for a planar interface; i.e., $c_{\text{ref}} = 1/k$. We assume that the interface has reflective symmetry so that

$$\frac{\partial c_m}{\partial x} = \frac{\partial c_s}{\partial x} = \frac{\partial h}{\partial x} = 0, \quad x = 0 \text{ and } x = \lambda \ . \tag{31}$$

The values of the dimensionless groups used in the analysis described here are for the two sets used in many previous calculations; the parameters for an alloy Pb-Sn, with $R_m = 0$, as used in previous numerical simulations[3–6] and the parameters for the organic alloy succinonitrile-acetone (SCN-ACE) alloy that is used in many thin-film solidification experiments;[12,16] these parameters are listed in Table I.

TABLE I. Dimensionless groups and coefficients for amplitude equations for Pb-Sb and succinonitrile-acetone systems

Value	Pb-Sb	Succinonitrile-acetone
Segregation coefficient, k	0.4	0.1
Dimensionless liquidus slope, m	-1.67×10^{-4}	-1.34×10^{-3}
Capillary Constant, Γ	8.2×10^{-7}	1.9×10^{-6}
Diffusivity Ratio, R_m	0	0.05
Temperature Gradient, G	4.5×10^{-5}	4.5×10^{-5}
P_d	0.2804	0.0761
ω_d	0.9593	0.8039
λ_d	6.5501	7.8157
$\hat{F}_\omega(\omega_d,P_d)$	1.6452×10^{-2}	4.4552×10^{-4}
$\hat{F}_P(\omega_d,P_d)$	7.4560×10^{-1}	7.5997×10^{-1}
$\hat{F}_\omega(2\omega_d,P_d)$	-2.0744×10^{-2}	-5.3260×10^{-4}
$\hat{F}_P(2\omega_d,P_d)$	1.7011	1.5645
b_1	1.2418×10^{-1}	-1.2804×10^{-3}
b_2	-3.2992×10^{-2}	-2.3380×10^{-3}
c_1	-6.3402×10^{-1}	1.8039×10^{-4}
c_2	-2.1308×10^{-2}	-8.6721×10^{-4}
c_3	-5.7236×10^{-1}	1.818×10^{-2}
c_4	-2.9155×10^{-1}	-2.1321×10^{-3}

B. Center manifold analysis

Amplitude equations of the form of Eqs. (14) have been derived previously for models of thin-film directional solidification by Haug[7,8] and Rappel and Riecke.[23] However, Haug's analysis was restricted to R_m values of either 1 or 0 and is not generally applicable. Rappel and Riecke studied the evolution of traveling wave states that exist close to the codimension-two point when the boundary conditions are taken to be periodic instead of reflective. They did not consider the evolution of the Hopf bifurcation with reflective boundary conditions, which is of particular interest here. The derivation of the amplitude equations is outlined very briefly here and is given in more detail by Tsiveriotis.[22] The algebra necessary for derivation of the coefficients in Eqs. (14) is complex and was performed using the symbolic manipulator MAPLE.[24]

The solutal model is put in local form by defining reduced variables formed by subtracting off the steady-state solution for a flat interface, which is given by

$$\begin{bmatrix} h^{(ss)}(x) \\ c_m^{(ss)}(x,y) \\ c_s^{(ss)}(x,y) \end{bmatrix} = \begin{bmatrix} 0 \\ 1+[(1-k)/k]\exp(-Py) \\ 1 \end{bmatrix} . \tag{32}$$

These new variables are

$$\begin{bmatrix} h(x,t) \\ c_m(x,y,t) \\ c_s(x,y,t) \end{bmatrix} = \begin{bmatrix} \hat{h}(x,t) \\ \hat{c}_m(x,y,t) \\ \hat{c}_s(x,y,t) \end{bmatrix} + \begin{bmatrix} h^{(ss)}(x) \\ c_m^{(ss)}(x,y) \\ c_s^{(ss)}(x,y) \end{bmatrix} . \tag{33}$$

Because the solute equations are linear in the concentration fields (c_s,c_m), the equations for the reduced variables are unchanged. The modified forms of Eqs. (29) and (30) are

$$P(k-1)[\hat{c}_m+1-\exp(-P\hat{h})]+\frac{1}{(1+\delta)^2}(1-R_m)\frac{\partial\hat{h}}{\partial x}\frac{\partial\hat{c}_m}{\partial x}-R_m\frac{1}{(1+\delta)^2}\frac{\partial\hat{h}}{\partial x}\frac{\partial\hat{c}_m}{\partial x}-\frac{\partial\hat{c}_m}{\partial y}+R_m\frac{\partial\hat{c}_s}{\partial y}$$
$$=\left[\hat{c}_m+1+\left[\frac{1}{k-1}\right]\exp(-P\hat{h})\right](1-k)\frac{\partial\hat{h}}{\partial t} , \tag{34}$$

$$G\hat{h}-\frac{m(k-1)}{k}[1-\exp(-P\hat{h})]-m\hat{c}_m-\Gamma\frac{1}{(1+\delta)^2}\frac{\partial^2\hat{h}}{\partial x^2}\left[1+\frac{1}{(1+\delta)^2}\left[\frac{\partial\hat{h}}{\partial x}\right]^2\right]^{-3/2} . \tag{35}$$

Amplitude equations that govern the weakly nonlinear dynamics of the interface are derived from these equations using the forms of $(\hat{h},\hat{c}_m,\hat{c}_s)$, which satisfy the field equations (28) and the symmetry conditions (31). The concentrations in the melt and solid at the interface are linked by the phase equilibrium condition in the transformed variables. It is interesting to note that expanding the exponential $\exp(-P\hat{h})$ in Eq. (34) in powers of $\hat{h}$ leads to $\hat{h}^2$ as the leading order nonlinear term, identically to the form that appears in the modified Swift-

Hohenberg equation (1).

The linear stability equations are recovered by substituting Eqs. (33) into the solutal model, Eqs. (28)–(31), and expanding for small amplitude disturbances. Each disturbance to the interface (and the field variables) is represented by the normal modes $h(x,\tilde{t}) = \hat{h}\exp(\sigma t + i\omega x)$. The result of the analysis is a dispersion relation

$$\sigma = \hat{F}(\omega, P) \tag{36}$$

that predicts the linear stability of the planar interface to disturbances with spatial wave number ω. Neutral stability corresponds to $\sigma = 0$ and the neutral stability curve has the parabolic form shown in Fig. 1. The codimension-two bifurcation again appears at $\omega = \omega_d$ and $P = P_d$.

Using the analysis of the MSH as a guide, the reduced variables are expanded in the five spatial modes, corresponding to the lateral wave numbers $(0, \omega_d, 2\omega_d, 3\omega_d, 4\omega_d)$ as

$$\begin{bmatrix} \hat{h}(x,t) \\ \hat{c}_m(x,y,t) \\ \hat{c}_s(x,y,t) \end{bmatrix} = \sum_{k=0}^{4} \begin{bmatrix} h_k \\ c_{m,k}\exp(-\omega_1^* y) \\ c_{s,k}\exp(-\omega_s^* y) \end{bmatrix} \cos(k\omega_d x) , \tag{37}$$

where

$$\begin{aligned} \omega_1^* &\equiv P_d/2 + \sqrt{(P_d/2)^2 + \omega_d^2} , \\ \omega_d^* &\equiv P_d/(2R_m) + \sqrt{(P_d/2)^2 + (\omega_d R_m)^2} . \end{aligned} \tag{38}$$

The Eqs. (37) for the concentration fields satisfy the solute equations (28), so that the unknown coefficients are fully determined by the Eqs. (29) and (30), written in the reduced variables.

The center manifold reduction described in Sec. II A is used to reduce these equations to amplitude equations that govern the dynamics of the interface near the codimension-two wave number $\omega = \omega_d$ and for $|P - P_d| \ll 1$. The distance from the codimension-two state is controlled by the parameter δ, which is defined identically to the definition (4) used in the analysis of the MSH equation. Equations (28) are expanded using a domain perturbation expansion to include terms that are third-order accurate in (h_1, h_2), second-order in (h_0, h_3, h_4), and first-order in δ and $(P - P_d)$. Projections with respect to the spatial functionality $\{\cos(i\omega_d x)\}$ are used to reduce the interface equations to ten algebraic relations that are resolved for the coefficients in the concentration expansions in terms of the $\{h_i\}$. These equations are substituted in to the expansion for the interfacial solute balance, Eq. (29), which is expanded to $\mathbf{O}(h_1, h_2)^3$, $\mathbf{O}(h_0, h_3, h_4)^2$, $\mathbf{O}(\delta)$, and $\mathbf{O}(P - P_d)$, to give five amplitude equations for the coefficients in the interface shape. These equations are reduced to two amplitude equations by the center manifold approach, in a manner exactly analogous to the steps used for the MSH equation. These equations are written as

$$\frac{dh_1}{dt} = [-\hat{F}_\omega(\omega_d, P_d)\omega_d\delta + \hat{F}_P(\omega_d, P_d)(P - P_d)]h_1 + b_1 h_1 h_2 + c_1 h_1 h_2^2 + c_2 h_1^3 \tag{39a}$$

$$\frac{dh_2}{dt} = [-\hat{F}_\omega(2\omega_d, P_d)2\omega_d\delta + \hat{F}_P(2\omega_d, P_d)(P - P_d)]h_2 + b_2 h_1^2 + c_3 h_1^2 h_2 + c_4 h_2^3 \tag{39b}$$

where the subscripts, e.g., $\hat{F}_\omega(\omega_d, P_d)$, signify partial differentiation of the dispersion equation. The expressions for the coefficients are too complex to be given here; they are available in Ref. 22 in the form of Fortran functions generated directly by MAPLE.[24] The values of the coefficients computed using the thermophysical properties for the Pb-Sb and SCN-ACE systems are listed in Table I. The predictions of the asymptotic analysis are described in Sec. IV.

C. Numerical simulation methods

The predictions of the asymptotic analysis described above are compared to numerical analysis of the free- and moving-boundary problems for the steady-state and time-periodic solutions of the solutal model. The algorithms for solution as described in Refs. 22 and 25 are only sketched here. The unknown interface shape is accounted for in the numerical method by introducing a nonorthogonal mapping that transforms the free-boundary problem to a fixed domain where the boundary between melt and solid corresponds to one boundary of the domain. We use the elliptic mapping method described in Ref. 25 and that was developed for the computation of solidification interfaces. The partial differential equations for the concentration fields and the mapping equations for the coordinate transformation are discretized by Galerkin finite-element methods, as described in Ref. 25. The Gibbs-Thomson equation, Eq. (30), is used to compute the coordinate transformation on the portion of the boundary of the transformed domain that corresponds to the melt-crystal interface.

The Galerkin's methods leads to a large set of nonlinear algebraic equations for calculation of steady-state interface shapes and to a system of differential-algebraic equations (DAE's) for the description of time-dependent states. The steady-state equations are solved by Newton's method, augmented with computer-implemented bifurcation analysis for tracking multiple solutions. Time-dependent simulations use second-order accurate backward difference approximations with variable time step to solve the DAE's; see Ref. 21 for details.

IV. COMPARISON OF ANALYSIS AND SIMULATION

Finite-element calculations were carried out for both sets of thermophysical properties in Table I. The comparison between the calculation of steady-state cell shapes and the predictions of the amplitude equations is described in Sec. IV A; time-periodic states predicted by the asymptotic analysis and the finite-element simulations are reported in Sec. IV B and IV C.

A. Steady-state solutions

Finite-element calculations of steady-state cell shapes are represented by the bifurcation diagrams in Fig. 6 for the Pb-Sb alloy and sample widths equal to 0.72, 0.855, and 1.1 of the wavelength λ_d for the codimension-two bifurcation; the symmetry of the interface shapes for each solution family is shown schematically in the first diagram. Primary and secondary bifurcation points between steady-state solution families and Hopf bifurcations to time-periodic solutions are shown; the solution structure agrees qualitatively with the structure expected from the amplitude equations for coefficients which satisfy $b_1 b_2 < 0$ and $c_4 < 0$, as is the case for this parameter set. For this set of thermophysical properties, there is a Hopf bifurcation point on the mixed solution family, that appears adjacent to the secondary bifurcation point for wavelengths greater than the critical value λ_d. The time-periodic solutions that evolve from this point are discussed in Sec. IV B.

The numerical calculations are compared directly to the predictions of the amplitude equations (37) in Fig. 7, where the bifurcation diagrams computed for the Pb-Sb properties are shown for the value $\delta = -0.145$ of the imperfection parameter. The agreement is quantitative between the two calculations. Note that the secondary bifurcation between the two primary solution families occurs at lower values of amplitude, i.e., smaller Δ, than in Fig. 6 because the distance to the codimension-two point is smaller.

Time integration of the linear stability equations formed about the numerically computed steady-state solutions was used to assess the stability of these states; these results correspond identically to the predictions for the MSH equation for the appropriate sign of δ. For $\lambda = 0.855\lambda_d$ ($\delta > 0$) the mixed solution family is everywhere stable from the point of bifurcation with the planar state to the secondary bifurcation where it connects to the pure solution. Alternatively, the pure solution family contains unstable interfaces up to the secondary bifurcation with the mixed family, but these shapes are stable for larger values of P.

Similar calculations were carried out for the thermophysical properties for the succinonitrile-acetone alloy and are shown in Figs. 8 and 9. The connectivity of the solution families is qualitatively different than for the Pb-Sb thermophysical properties. As predicted by the amplitude equations derived by center manifold theory for the case $b_1 b_2$, there is no connectivity between the primary solution families at low amplitudes, i.e., $\Delta \ll 1$. This point is reinforced by the comparison between the finite-element calculations and the predictions of the amplitude equations shown in Fig. 9 for $\delta = -0.053$. Note that no connectivity between the two families is predicted for cells with amplitudes satisfying $\Delta < 0.5$. However, at large amplitudes, the pure and mixed solution families do connect in the finite-element calculations. This connectivity is not predicted by the amplitude equations, which are valid to cubic-order; hence the connectivity demonstrated in Fig. 8 must be a higher-order effect.

B. Time-periodic solutions for Pb-Sb alloy

The Hopf bifurcation point that arises in the solution structure for the Pb-Sb thermophysical parameters gives rise to a family of time-periodic solutions. The form and stability of these states is computed by time integration of the finite-element discretization of the solutal model. For $\lambda = 1.1\lambda_d$, time periodic solutions start at the Hopf bifurcation point $P = P_{\text{Hopf}} = 0.279\,30$ and evolve supercritically in P, as shown in Fig. 10. Oscillatory states were only computed for a very short range of growth rates, $0.279\,30 < P < 0.279\,45$; attempts to compute a stable oscillatory state for $P = 0.279\,48$ produced a transient solution that evolved back to the pure steady-state form at that value of P; this result suggested that the family of time-periodic states has lost temporal stability, either by reversing directions at a limit point, or by a subcritical Hopf bifurcation with another frequency. The calculations cannot separate between these two scenarios for the evolution. Even in this small range of growth rate the time-periodic states develop very nonlinear character. The amplitude of the cell deformation increases dramatically, as shown in Fig. 10, and the period of the oscilla-

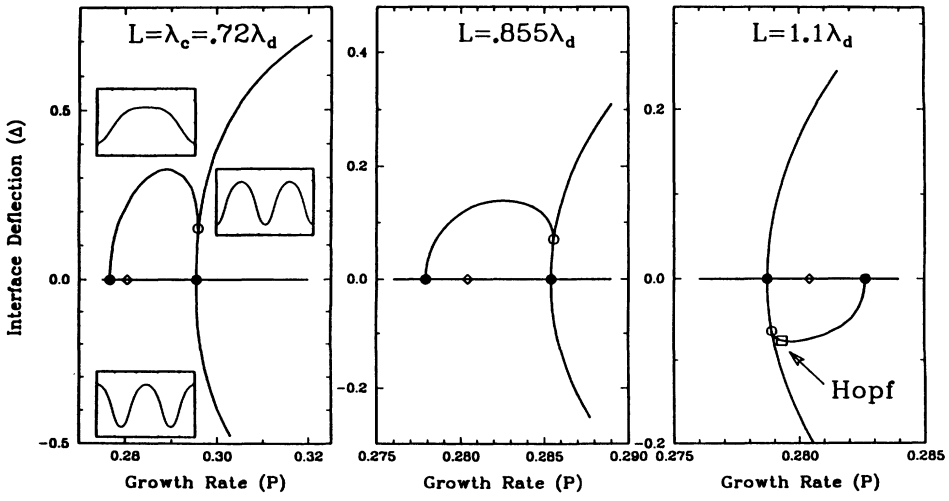

FIG. 6. Bifurcation diagrams computed by finite-element analysis for the thermophysical properties of the Pb-Sb alloy and for cellular wavelengths close to the codimension-two bifurcation point $\lambda = \lambda_d$. The symbols represent primary (●) and secondary (○) bifurcation points between families of steady-state solutions and (□) Hopf bifurcations to families of time-periodic states.

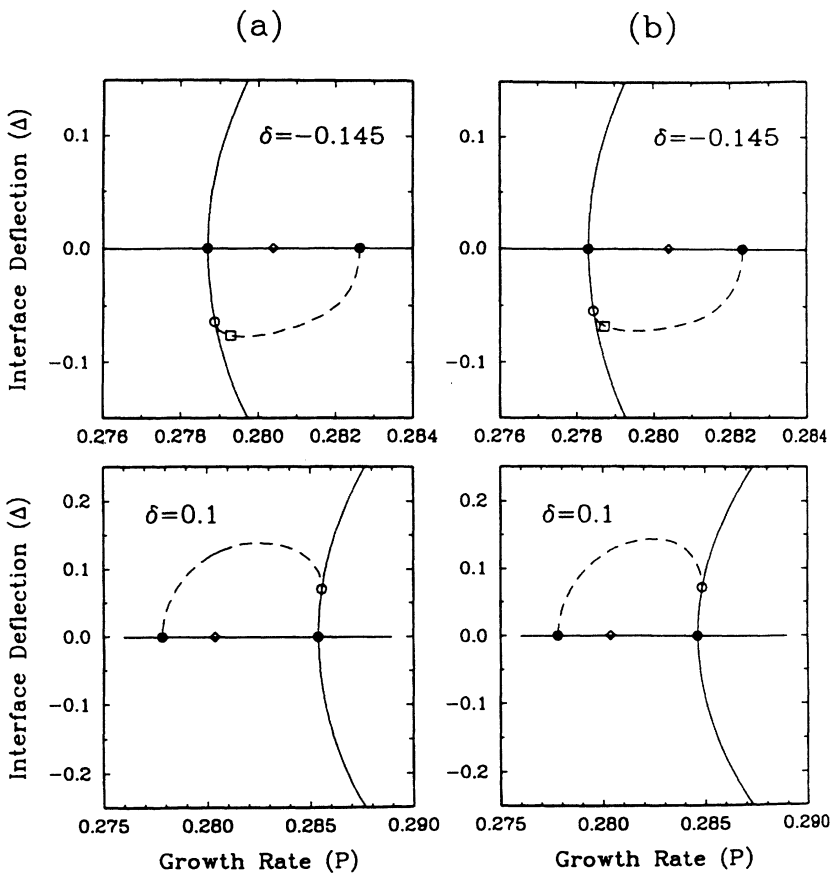

FIG. 7. Comparison between bifurcation diagrams computed by (a) finite-element analysis of the solutal model and (b) analysis of the amplitude equations (37) for the thermophysical properties of the Pb-Sb alloy. Solid and dashed curves represent families of steady-state cells with ω and 2ω symmetry, respectively. The symbols represent primary (●) and secondary (○) bifurcation points between families of steady-state solutions and (□) Hopf bifurcations to families of time-periodic states.

tion increases by 40%; see Fig. 11.

The changes in the character of the oscillations from the sinusoidal dynamics predicted close to the Hopf point (a) to large amplitude oscillations (b) and (c), and the transient back to the steady-state solution family (d) are displayed in Fig. 12 by the time histories of the maximum interface deflection Δ_{max} and contour maps of the interface shape. The amplitudes of the cells along the interface oscillate in time. Close to the Hopf point ($P=0.7930$) these oscillations are approximately sinusoidal, but quickly grow in amplitude and begin to include higher harmonics. Note that the period of the oscillation is $O(10^3)$ diffusion time scales. The dependence of the period on the spatial wavelength of the cells is plotted in Fig. 12 as computed for four values of δ near the Hopf bifurcation points. The period increases with decreasing δ and approximately obeys the asymptotic scaling, Eq. (27), predicted by the analysis of the amplitude equations.

For the case of the SCN-ACE alloy, the asymptotic

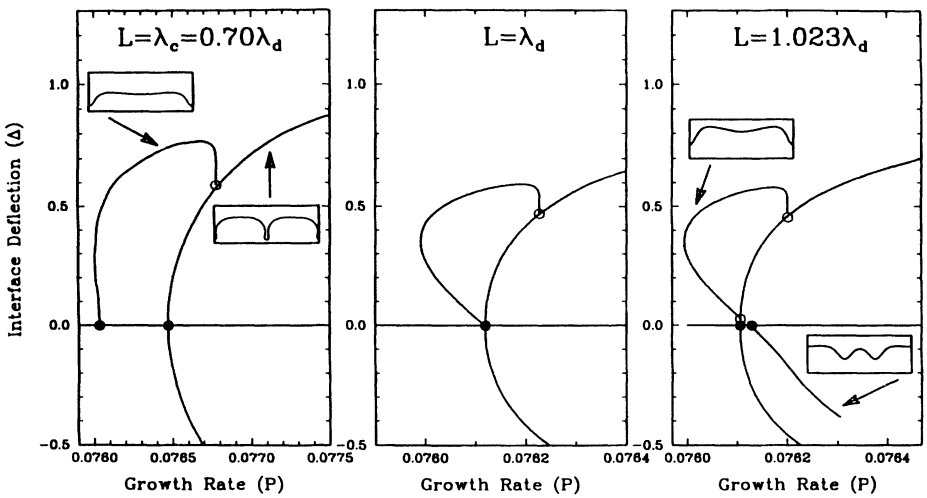

FIG. 8. Bifurcation diagrams computed by finite-element analysis for the thermophysical properties of the succinonitrile-acetone alloy and for cellular wavelengths close to the codimension-two bifurcation point $\lambda=\lambda_d$. The symbols represent primary (●) and secondary (○) bifurcation points between families of steady-state solutions and (□) Hopf bifurcations to families of time-periodic states.

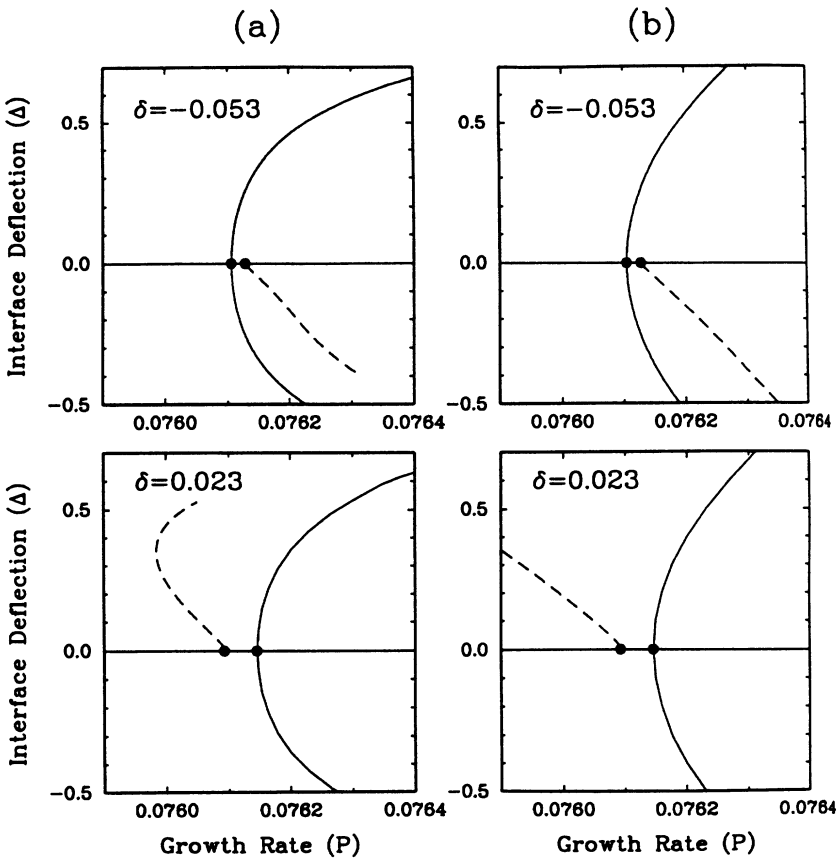

FIG. 9. Comparison between bifurcation diagrams computed by (a) finite-element analysis of the solutal model and (b) analysis of the amplitude equations (37) for the thermophysical properties of the succinonitrile-acetone alloy. Solid and dashed curves represent families of steady-state cells with ω and 2ω symmetry, respectively. The symbols represent primary (●) and secondary (○) bifurcation points between families of steady-state solutions and (□) Hopf bifurcations to families of time-periodic states.

analysis predicts no Hopf bifurcation on the mixed solution family. Time-dependent numerical simulations confirm this prediction for small interface deflections and for conditions close to the codimension-two point. Nevertheless, at large amplitudes and at finite distances from the codimension-two point a new highly localized mode for oscillations has been discovered which involves the pulsation of the narrow grooves that form between the cells; these states are described in Ref. 26 and cannot be connected to the weakly nonlinear analysis for nearly planar states.

V. DISCUSSION

The analysis and calculations presented here gives a theoretical explanation for the appearance of long-time-

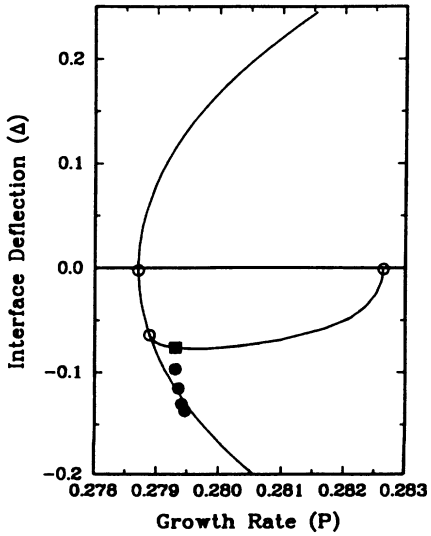

FIG. 10. Expanded view of bifurcation diagram for Pb-Sb system with $\lambda = 1.1\lambda_d$ showing the Hopf bifurcation point (■) and family of time-periodic solutions (●).

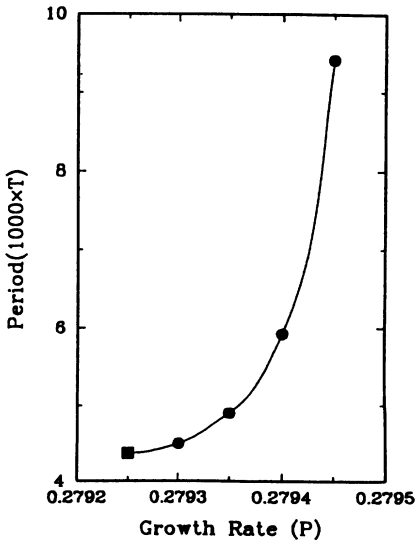

FIG. 11. Computed period of time-periodic solutions as a function of P for Pb-Sb system with $\lambda = 1.1\lambda_d$.

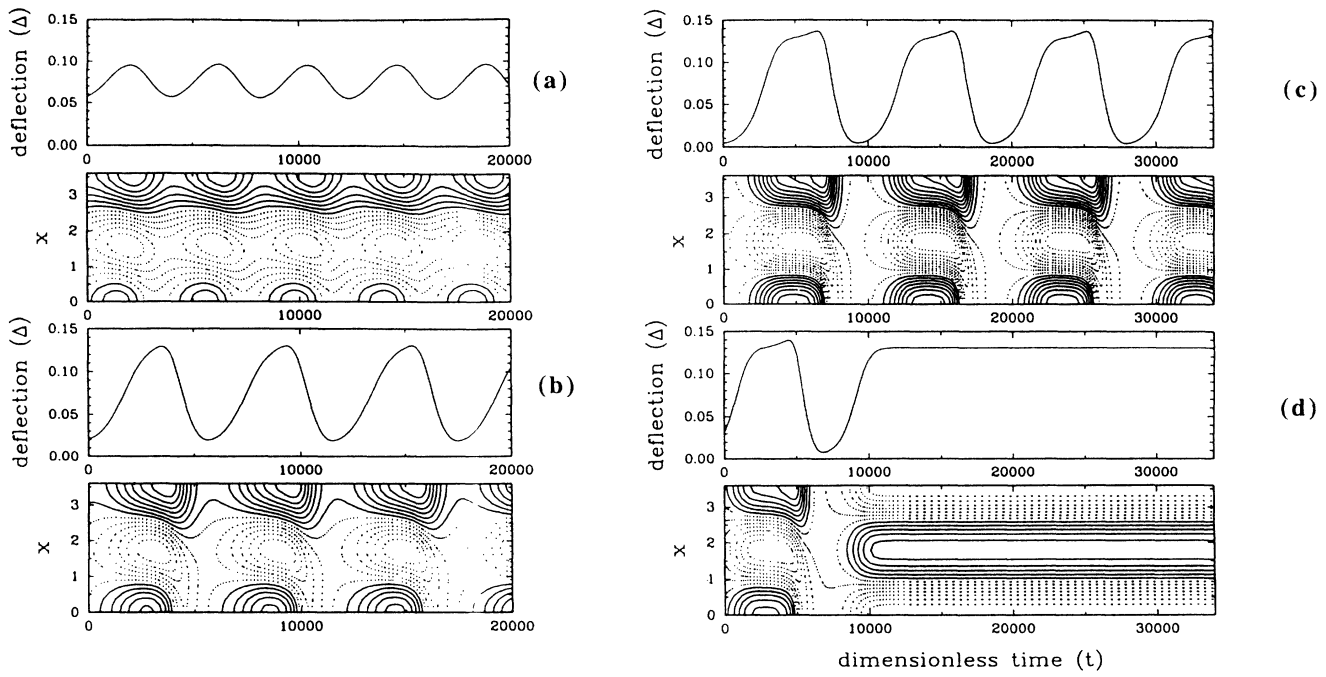

FIG. 12. Time-dependent dynamics of sample simulations for time-periodic states for calculations at dimensionless growth rates P of (a) 0.7930, (b) 0.7940, (c) 0.7945, and (d) 0.7948 for the Pb-Sb system with $\lambda = 1.1\lambda_d$. For each case, both the evolution of the overall interface deflection Δ and contours of the deflection of the interface are shown as a function of time.

scale, temporal dynamics in thin-film directional solidification. A mechanism is identified for the dynamics, whereby the proximity to the codimension-two bifurcation corresponding to 2:1 spatial resonance between the wave numbers of cells leads to time-periodic solutions. These time-periodic states are seen as oscillations in the amplitudes of neighboring cells and arise as an effect of the quadratic nonlinearity that describes the 2:1 spatial resonance near the wave number λ_d, corresponding to the codimension-two bifurcation point. Asymptotic analysis of the amplitude equations for quadratic resonance of these modes shows that the appearance of the Hopf bifurcation is connected to the connectivity of the steady-state solution families that evolve from the planar state and can be predicted from the signs of coefficients in the amplitude equations. Also the temporal periods of these time-periodic states are predicted to scale as $\delta^{-3/2}$, where δ measures the distance of the wavelength from λ_d. Finite-element analysis of the two-sided solutal model reproduces the results of the asymptotic analysis for the Pb-Sb alloy; moreover, finite amplitude time-periodic states are computed that evolve from this Hopf bifurcation.

The relevance of these results to the dynamics seen in thin-film directional solidification experiments relies on the flatness of the neutral stability curves that are typical for these systems. Computations[4–6] and experiments[12,16] have demonstrated that the flatness of the neutral curve causes codimension-two interactions which increase the apparent wave number of the interface for growth rates only slightly above the critical point. Although nonlinear dynamics caused by these couplings and by other interactions prevent a system with multiple cells from selecting a unique spatial wavelength, the system evolves such that it is always close to points of spatially resonant interaction for growth rates near $V_c(\omega_c)$.

The dynamics for single cells in directional solidification, as described here, is not chaotic because only interactions between two modes are considered. In the large collections of cells that comprise a solidification front, multiple resonant interactions of the 2:1 type, as well as other modal interactions characterized by $(n+1):n$ give rise to the nonlinear couplings needed to achieve spatiotemporal chaos along the solidification front. In addition, for larger samples, with set growth rate, the perturbation parameter δ, which measures the distance from codimension-two points, can dynamically vary because of the expansion and contraction of cells along the front, thereby introducing additional complexity into the dynamics.

ACKNOWLEDGMENTS

The research described here was supported by the Microgravity Sciences and Applications Program of the National Aeronautics and Space Administration and by a grant of computer time from the Pittsburgh Supercomputer Center, which is supported by the National Science Foundation.

[1]W. W. Mullins and R. F. Sekerka, J. Appl. Phys. **34**, 444 (1964).
[2]D. J. Wollkind and L. A. Segal, Philos. Trans. R. Soc. London **268**, 351 (1970).
[3]L. H. Ungar and R. A. Brown, Phys. Rev. B **29**, 1367 (1984).
[4]N. Ramprasad and R. A. Brown, Phys. Rev. B **38**, 583 (1988).
[5]M. J. Bennett and R. A. Brown, Phys. Rev. B **39**, 11 705 (1989).
[6]M. J. Bennett, K. Tsiveriotis, and R. A. Brown, Phys. Rev. B **45**, 9562 (1992).
[7]P. Haug, Phys. Rev. A **35**, 4364 (1987).
[8]P. Haug, Phys. Rev. A **40**, 844 (1989).
[9]G. Dangelmayr and D. Armbruster, Cont. Math. **56**, 53 (1986).
[10]D. Armbruster and G. Dangelmayr, Math. Proc. Cambridge Philos. Soc. **101**, 167 (1987).
[11]B. A. Malomed and M. I. Tribelsky, Physica D **14**, 67 (1984).
[12]T. C. Lee, K. Tsiveriotis, and R. A. Brown, J. Cryst. Growth **121**, 536 (1992).
[13]W. Eckhaus, *Non-Linear Stability Theory* (Springer-Verlag, New York, 1965).
[14]K. Tsiveriotis and R. A. Brown, Phys. Rev. Lett. **63**, 2048 (1989).
[15]M. R. E. Proctor and C. A. Jones, J. Fluid Mech. **188**, 301 (1988).
[16]T. C. Lee and R. A. Brown, Phys. Rev. B **47**, 4937 (1993).
[17]J. Swift and P. C. Hohenberg, Phys. Rev. A **15**, 319 (1977).
[18]J. Carr, *Applications of the Center Manifold Theory* (Springer-Verlag, New York, 1981).
[19]J. Carr and R. G. Muncaster, J. Diff. Eqs. **50**, 260 (1983).
[20]J. Carr and R. G. Muncaster, J. Diff. Eqs. **50**, 280 (1983).
[21]J. Guckenheimer and P. Holmes, *Nonlinear Oscillations, Dynamical Systems and Bifurcations of Vector Fields* (Springer-Verlag, New York, 1983).
[22]K. Tsiveriotis, Ph.D. thesis, Massachusetts Institute of Technology, Cambridge, MA, 1992.
[23]W. J. Rappel and H. Riecke, Phys. Rev. A **45**, 846 (1991).
[24]B. Char, K. O. Gheddes, G. H. Gonnet, B. L. Leong, M. B. Monogan, and S. M. Watt, *First Leaves: A Tutorial Introduction to Maple V* (Springer-Verlag, New York, 1992).
[25]K. Tsiveriotis and R. A. Brown, Inter. J. Numer. Meths. Fluids **14**, 981 (1992).
[26]K. Tsiveriotis and R. A. Brown, Phys. Rev. B **48**, 13 495 (1993).